

Ultraviolet Signatures of the Multiphase Intracluster and Circumgalactic Media in the RomulusC Simulation

Iryna S. Butsky,^{1*} Joseph N. Burchett,² Daisuke Nagai,^{3–5} Michael Tremmel,^{3,5}
Thomas R. Quinn,¹ and Jessica K. Werk¹

¹ *Department of Astronomy, University of Washington, Seattle, WA, 98195-1580, USA*

² *Department of Astronomy and Astrophysics, University of California, Santa Cruz, USA*

³ *Department of Physics, Yale University, New Haven, CT 06520, USA*

⁴ *Department of Astronomy, Yale University, New Haven, CT 06520, USA*

⁵ *Yale Center for Astronomy and Astrophysics, New Haven, CT 06520, USA*

Accepted XXX. Received YYY; in original form ZZZ

ABSTRACT

Quasar absorption-line studies in the ultraviolet (UV) can uniquely probe the nature of the multiphase cool-warm ($10^4 < T < 10^6$ K) gas in and around galaxy clusters, promising to provide unprecedented insights into 1) interactions between the circumgalactic medium (CGM) associated with infalling galaxies and the hot ($T > 10^6$ K) X-ray emitting intracluster medium (ICM), 2) the stripping of metal-rich gas from the CGM, and 3) a multiphase structure of the ICM with a wide range of temperatures and metallicities. In this work, we present results from a high-resolution simulation of a $\sim 10^{14} M_{\odot}$ galaxy cluster to study the physical properties and observable signatures of this cool-warm gas in galaxy clusters. We show that the ICM becomes increasingly multiphased at large radii, with the cool-warm gas becoming dominant in cluster outskirts. The diffuse cool-warm gas also exhibits a wider range of metallicity than the hot X-ray emitting gas. We make predictions for the covering fractions of key absorption-line tracers, both in the ICM and in the CGM of cluster galaxies, typically observed with the Cosmic Origins Spectrograph aboard the Hubble Space Telescope (HST). We further extract synthetic spectra to demonstrate the feasibility of detecting and characterizing the thermal, kinematic, and chemical composition of the cool-warm gas using H I, O VI, and C IV lines, and we predict an enhanced population of broad Ly α absorbers tracing the warm gas. Lastly, we discuss future prospects of probing the multiphase structure of the ICM beyond HST.

Key words: galaxies:clusters:general – galaxies:clusters:intracluster medium – galaxies:halos – methods:numerical

1 INTRODUCTION

Galaxy clusters form ecosystems on the largest mass and spatial scales and serve as unparalleled laboratories for galaxy evolution and extreme magnetohydrodynamic phenomena. Clusters are marked by hot, X-ray emitting, intracluster media (ICM) that serve as records of cluster dynamics and chemical enrichment history. All infalling galaxies are subject to the punishing conditions of the ICM throughout their journey, while individual galaxies are embedded in diffuse, multiphase circumgalactic media (CGM) that mediate the ‘baryon cycle’, consisting of galactic outflows and accre-

tions of gas that ultimately dictate star formation activity and the transport of heavy elements (Tumlinson et al. 2017). Thus, it is the interplay between the ICM and CGM that manifests in many aspects of cluster gas physics, and understanding the complex thermodynamic and chemical structures of the ICM is critical to understanding the evolution of cluster galaxies (see Kravtsov & Borgani 2012; Walker et al. 2019, for reviews).

Galaxy clusters are also sites of extraordinary galaxy transformation. On average, cluster galaxies are more likely to be quenched and to have less gas in their interstellar medium (ISM) (Davies & Lewis 1973; Dressler 1980; Sandage et al. 1985) than isolated field galaxies. There are several ways in which the cluster environment may contribute to this gas shortage, although the dominant mech-

* E-mail: ibutsky@uw.edu

anisms are still debated (Fraser-McKelvie et al. 2018): a combination of tidal stripping by the massive center galaxy (Moore et al. 1996; Lake et al. 1998; Wang et al. 2004), high-speed fly-bys, and mergers with other galaxies (Toomre & Toomre 1972; White & Rees 1978; Roediger et al. 2015) or ram-pressure stripping from the ICM (Gunn & Gott 1972; Fumagalli et al. 2014). This cool, metal-rich, stripped gas contributes to the clumpy morphology in cluster outskirts before ultimately mixing with the ICM (Tonnesen et al. 2007; Jáchym et al. 2014). Recent studies have also shown that the CGM of cluster galaxies is quite deficient relative to their more isolated counterparts (Yoon & Putman 2013; Burchett et al. 2018), although the samples remain small and it is less clear where this transformation occurs. If galaxies’ CGM are stripped early upon infall, this may lead to a much slower quenching process than rapid stripping of the interstellar medium (ISM) (Zinger et al. 2018).

To date, X-ray and microwave measurements of the thermodynamic and metallicity profiles of the ICM have been critical towards determining the physics governing structure formation (Walker et al. 2019; Mroczkowski et al. 2019, for reviews), chemical enrichment of the ICM (Werner et al. 2013; Urban et al. 2017; Mernier et al. 2018, for a review), and cosmological models (Allen et al. 2011; Pratt et al. 2019, for reviews). Modern cosmological simulations of galaxy cluster formation predict that the outskirts of galaxy clusters is a cosmic-melting pot, where the structure formation processes, such as mergers and gas accretion (Lau et al. 2015; Zinger et al. 2016), generate clumpy (Nagai & Lau 2011; Zhuravleva et al. 2013; Vazza et al. 2013; Rasia et al. 2014) and turbulent (Lau et al. 2009; Nagai et al. 2013; Nelson et al. 2014) hot X-ray emitting ICM in the outskirts of galaxy clusters. In this work, we explore an alternative approach to studying the ICM and cluster galaxy CGM: probing the diffuse, cool-warm, gas that is virtually invisible to the observational techniques described above, using using absorption-line (UV) spectroscopy.

Rest-frame UV absorption-line spectroscopy studies have revolutionized our understanding of how the CGM influences and, conversely, is influenced by relatively isolated galaxies (e.g. Tumlinson et al. 2011; Tripp et al. 2011; Stocke et al. 2013; Werk et al. 2013; Bordoloi et al. 2014). Our picture of the CGM has transformed from that of a quiescent remnant of galaxy formation, to one of a turbulent, multiphase medium with a rich ionization and kinematic structure that plays a key role in galaxy evolution (Tumlinson et al. 2017). Similarly, UV observations of the cool-warm ICM have the potential to provide unprecedented insights to the thermodynamic, kinematic, and chemical properties of galaxy clusters. Directly observing the stripping of the CGM of infalling galaxies will place stringent constraints on 1) the dominant quenching mechanisms in high density environments, 2) the conditions and timescales that govern CGM stripping through interactions with the ICM, 3) the distribution of metals across all phases of the ICM, and 4) the role of feedback on the thermodynamic and chemical properties of the CGM. Additionally, UV-derived column density measurements and photoionization modeling can constrain the baryon fraction in the hot ($T > 10^6\text{K}$) X-ray emitting ICM to complement those estimates made using X-ray and microwave observations (Burchett et al. 2018; Ge et al. 2016; Wang & Walker 2014).

Several groups have successfully pioneered UV observations of the cool-warm gas in galaxy groups and clusters using *HST/COS* (e.g., Yoon et al. 2012; Johnson et al. 2015; Muzahid et al. 2017; Pointon et al. 2017; Yoon & Putman 2017; Burchett et al. 2018; Nielsen et al. 2018; Stocke et al. 2019), although the large samples of UV sightlines systematically probing cluster environments have not yet been obtained as exist for CGM samples. Next-generation UV telescopes (e.g., *LUVOIR*; Bolcar et al. 2017) have the potential to increase both the number of observable background sources (e.g., quasars (QSOs) and galaxies) and the sensitivity to lower column densities of cool-warm gas by orders of magnitude. We return to compare current and future capabilities later in Section 6.

In this work, we characterize the multiphase ICM using a high resolution simulation of a $\sim 10^{14}M_{\odot}$ cluster and make testable predictions for its observable properties, both with *HST-COS* and with future instruments. This work is organized as follows. In §2, we describe our methods, the ROMULUSC simulation of a galaxy cluster, and the tools integral to our analysis. In §3, we present evidence for a multiphase, metal-enriched ICM. In §4, we discuss the properties of the CGM of cluster galaxies. In §5, we demonstrate how observable signatures trace the physical conditions of the gas using synthetic spectra. In §6, we discuss the current and future prospects of observing the cool-warm gas in galaxy clusters. We summarize our results in §7.

Throughout this work, we divide the gas into four distinct phases: *cold* ($T < 10^4\text{K}$), *cool* ($10^4 < T < 10^5\text{K}$), *warm* ($10^5 < T < 10^6\text{K}$) and *hot* ($T > 10^6\text{K}$). This convention differs somewhat from that adopted elsewhere in the literature (e.g., Cen & Ostriker 1999), as we simply refer to the $10^5 < T < 10^6\text{K}$ phase as ‘warm’ rather than ‘warm-hot’. In the context of galaxy clusters, which contain an abundance of $T > 10^6\text{K}$ gas that is often simply deemed ‘hot’ in the literature, we feel that our nomenclature avoids ambiguity when discussing relationships between the phases. Thus, in this paper, we focus primarily on gas at cool-warm temperatures.

2 METHODS

2.1 The RomulusC Simulation

ROMULUSC (Tremmel et al. 2019) is a hydrodynamic cosmological zoom-in simulation of a $10^{14} M_{\odot}$ galaxy cluster run with the new Tree+Smoothed Particle Hydrodynamics (SPH) code, CHANGA (Menon et al. 2015). The zoom-in region is a Lagrangian region derived from the highest mass halo selected from a 50 Mpc uniform volume, dark matter-only simulation. ROMULUSC is among the highest resolution hydrodynamic cosmological simulations of a galaxy cluster run to date, with a Plummer equivalent gravitational force resolution of 250 pc (a 350 pc spline kernel is used), a maximum SPH resolution of 70 pc, and gas and dark matter mass resolutions of 2.12×10^5 and $3.39 \times 10^5 M_{\odot}$ respectively. At this resolution, ROMULUSC is one of only two cluster cosmological simulations currently in production that is capable of resolving the multiphase structure of gas in the ICM (see also Nelson et al. (2019)). Lower mass halos and galaxies, including their interaction with the ICM, are also followed

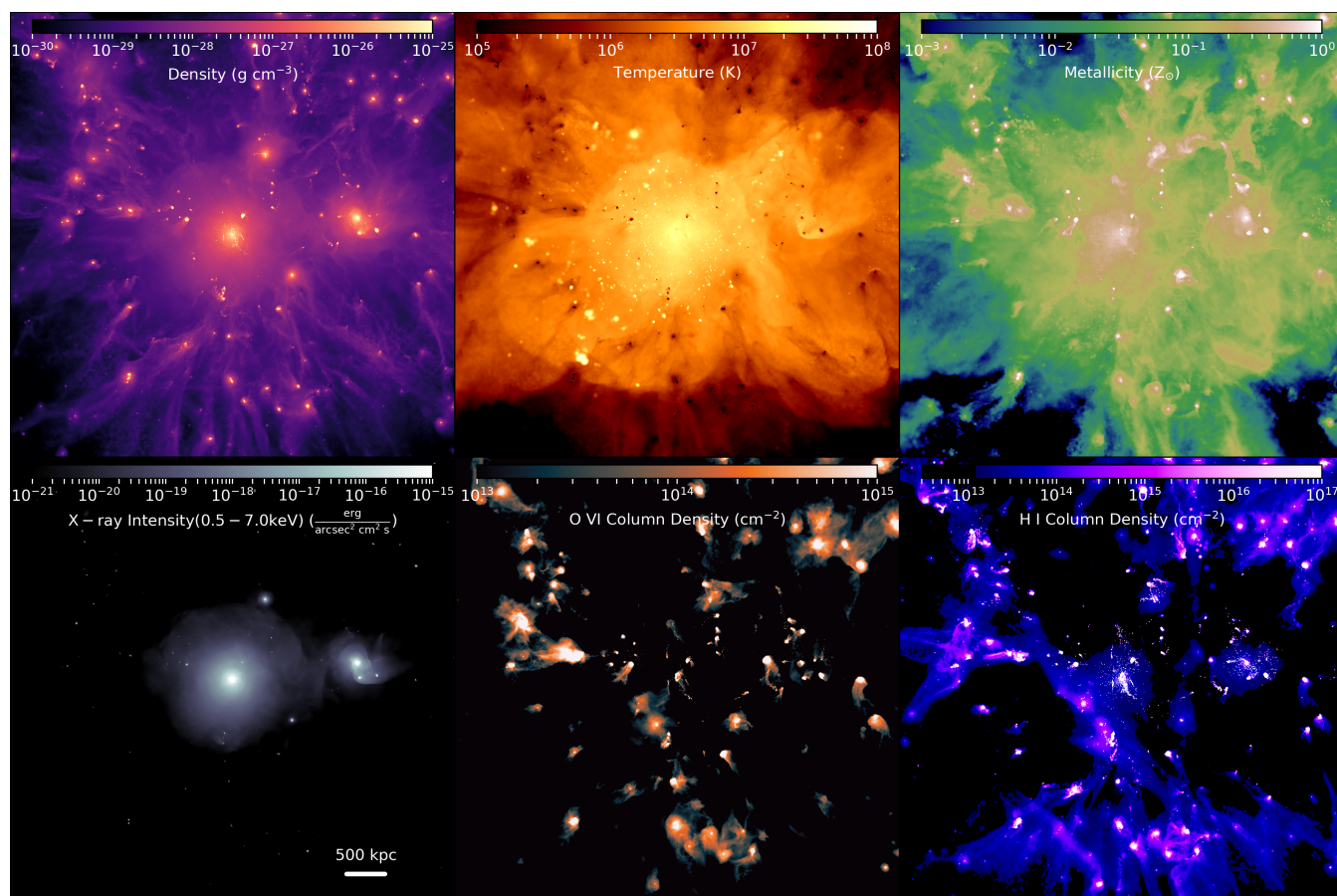


Figure 1. A 5×5 Mpc snapshot (in physical units) of the ROMULUSC simulation at $z = 0.31$. *Top row:* The density-weighted projections of gas density, temperature, and metallicity. *Bottom row:* The integrated X-ray intensity, O VI column density, and H I column density. The color scaling of the images in the bottom row is roughly consistent with the sensitivity of existing instruments. Compared to X-ray emission, the structure probed by UV absorption studies (O VI and H I column densities) better traces cluster outskirts and small-scale structure within the virial radius.¹

with greater detail than ever before. ROMULUSC resolves halos as small as $3 \times 10^9 M_\odot$ with at least 10^4 particles (spatial resolution sufficient for resolving ram-pressure stripping (Roediger et al. 2015)). As the CGM and ISM of infalling galaxies also contributes to the temperature, density, and metallicity distribution of gas within the ICM, ROMULUSC is able to provide a more complete picture of the ICM structure than other cluster simulations with more typical resolutions (often lower by factors of 10 or more in both mass and spatial resolution, see Table 1 in Tremmel et al. (2019)).

CHANGA uses sub-grid physics modules for star formation, stellar feedback, UV background with self-shielding, and low temperature metal cooling, that have been previously implemented and tested in GASOLINE (Wadsley et al. 2004, 2008, 2017). Supermassive black hole (SMBH) formation, dynamics, growth, and feedback is also included (Tremmel et al. 2015, 2017). Importantly, the simulation includes an updated implementation of turbulent diffusion (Wadsley et al. 2017), shown to be important for producing realistic entropy profiles in galaxy cluster cores (Wadsley et al. 2008) and metal distributions in galaxies (Shen et al. 2010). The combination of a gradient-based shock detector, time-dependent artificial viscosity, and an on-the-fly time-step adjustment system allows for a more realistic treatment of

both weak and strong shocks (Wadsley et al. 2017). Both the thermal and turbulent diffusion of metals is accounted for following Shen et al. (2010). Feedback from both stars and SMBHs is followed throughout the simulation. As in previous work for runs at this resolution (Stinson et al. 2006), star formation is assumed to occur with an efficiency of 15% in dense ($> 0.2 \text{ cm}^{-3}$), cold ($T < 10^4 \text{ K}$) gas on a characteristic timescale of 10^6 years. Supernova (SN) feedback follows the “blastwave” approach (Stinson et al. 2006), with each SN thermally coupling 0.75×10^{51} erg to the surrounding gas.

SMBHs are seeded based on local gas properties, assumed to form in very high density ($n_{\text{gas}} > 3 m_{\text{H}}/\text{cm}^3$), low metallicity ($Z < 3 \times 10^{-4} Z_\odot$) regions, which are self-consistently predicted to occur in the centers of low mass ($10^8 - 10^{10} M_\odot$) halos in the early Universe ($z > 5$). SMBHs grow through both mergers and accretion of gas via a modified Bondi-Hoyle prescription that accounts for both ad-

¹ While a number of ‘virial radius’ definitions exist in the literature, we generally adopt $r_{\text{vir}} = R_{200c}$, the radius within which the average density is 200x the critical density of the Universe. Other definitions may appear in the literature, and we provide the following the approximate scaling relation: $R_{500c} : R_{200c} : R_{200m} = 1 : 1.4 : 3$.

ditional support from angular momentum (Tremmel et al. 2017) and the unresolved multiphase structure in the ISM (Booth & Schaye 2009). A small fraction of the mass-energy of accreted material (0.2%) is transferred to nearby gas via thermal feedback and naturally results in large-scale outflows and has been shown to successfully regulate, and sometimes fully quench, star formation in massive galaxies (Pontzen et al. 2017; Tremmel et al. 2017, 2019).

The sub-grid models used here were derived from an extensive parameter calibration program, ensuring that the ROMULUS simulations create galaxies with realistic stellar masses, SMBH masses, gas content, and angular momentum (see Tremmel et al. 2017, for more details). Importantly, the sub-grid physics used in the ROMULUS simulations is tuned to reproduce realistic galaxy properties up to Milky Way-mass halos. Despite this, the simulation successfully predicts realistic SMBH and stellar masses for halos up to $2 \times 10^{13} M_{\odot}$. No effort was made to optimize the simulation to produce a realistic galaxy cluster, so all of the results from ROMULUSC are predictions from the simulation.

Note that ROMULUSC does not include metal-line cooling for temperatures above 10^4 K. This is one of the limitations of this simulation, as metal lines are an important coolant for warm-hot gas in the ICM. More specifically, at the gas temperatures ($T \sim 10^5$ K) and metallicities ($\sim 0.1 - 0.3 Z_{\odot}$) most relevant in this work, the extragalactic UV background dominates the heating/cooling balance, so the lack of metal-line cooling will result in cooling times that are a factor of $\sim 3 - 5$ too long (Shen et al. 2010). Furthermore, cooling in $10^4 - 5$ K gas is dominated by the He Ly α line, and primordial cooling does a reasonably good job of estimating metal-line cooling (Hopkins et al. 2018). We do include metal-line cooling for gas below 10^4 K, where contribution from metals becomes important.

At the cluster outskirts, where much of this work is focused, the cooling times are already quite long, even if metal cooling was accounted for, hence the inclusion of metal line cooling does not affect accretion of gas onto massive halos (van de Voort et al. 2011). The content of ions such as O VI in the ICM of ROMULUSC should therefore be robust to well within an order of magnitude. Closer to the BCG (and infalling cluster galaxies), the gas is just as sensitive to feedback physics as to the cooling model used (van de Voort et al. 2011). It is in this regime where the halo gas is strongly coupled to the ISM via feedback processes and it is not possible to separate the effects of high temperature cooling from feedback (and, therefore, ISM physics). Therefore, the robustness of the gas properties in the simulation is difficult to estimate.

At $z = 0$, the cluster is experiencing an on-going head-on merger with 1:8 mass ratio. The infalling halo is still outside R_{200} at $z = 0.3$ and begins to have an effect on the state of the ICM in the inner cluster at $z \lesssim 0.2$. The merger results in the destruction of the cool-core of the cluster (Chadayamuri et al., in prep). For most of the following analysis, in order to avoid the effects of a transient event, we focus on the state of the ICM when the cluster is still relaxed at $z = 0.31$, though we note that this is a higher redshift than the available observations we use for comparison. The virial radius of the cluster at this redshift is 810 kpc. The zoom-in Lagrangian region of ROMULUSC extends to ~ 3 Mpc from cluster center at $z = 0.3$. Since the physical state of the gas

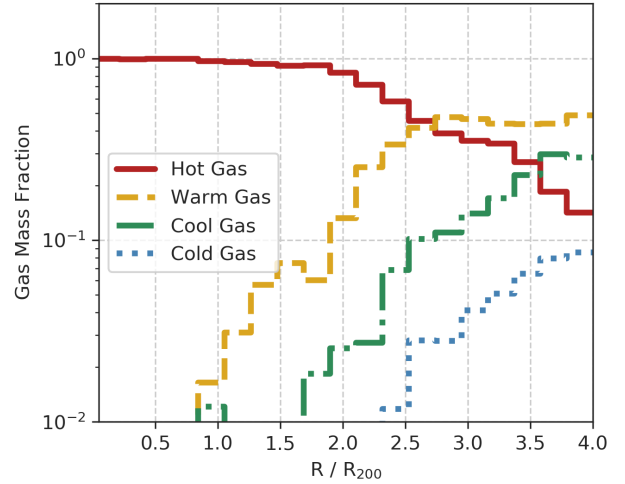


Figure 2. The mass fraction of cluster gas in the cold ($T < 10^4$ K), cool ($10^4 < T < 10^5$ K), warm ($10^5 < T < 10^6$ K), and hot ($T > 10^6$ K) phases as a function of 3D distance from the cluster center in the ROMULUSC simulation at $z = 0.31$. Although hot gas dominates within the virial radius of the cluster, warm and cool gas comprise the majority of the gas mass at the cluster outskirts.

near the outskirts of the Lagrangian region are subject to numerical effects, we limit our analysis to within this region. Hence, we do not expect this to affect any of our conclusions.

2.2 Ion Fields and Synthetic Absorption Spectra

We analyze our simulation data with a combination of YT (Turk et al. 2011), TRIDENT (Hummels et al. 2017), PYNBODY (Pontzen et al. 2013), and TANGOS (Pontzen & Tremmel 2018). In this section, we describe the process of transforming the physical quantities in simulation outputs to observable quantities and, ultimately, synthetic spectra.

Keeping track of individual atomic elements throughout the simulation is computationally expensive. Although some zoom-in simulations of low-mass galaxies have successfully tracked over 11 individual elements (e.g., Oppenheimer & Schaye 2013; Emerick et al. 2019), such detailed tracking is computationally infeasible, with current technologies, at the cluster scale. Instead, ROMULUSC explicitly tracks hydrogen, oxygen, and iron. The metallicity used here is a weighted sum of oxygen and iron based on solar abundance ratios (Asplund et al. 2009).

From the metallicity, we calculate specific ion abundances and their ionization states using TRIDENT¹, the first open-source, standardized tool for determining ion abundances and generating synthetic spectra from simulations. TRIDENT derives the abundance of each element in the simulation, n_X , by using the local metallicity and assuming a solar abundance by number². Then, the collisional ionization of each element is determined from the local gas tem-

¹ Trident is built as an extension of the widely-used analysis tool, YT (Turk et al. 2011) and is compatible with most astrophysical simulation codes.

² $n_X = n_H Z (n_X/n_H)_{\odot}$, where n_H and n_X are the number densities

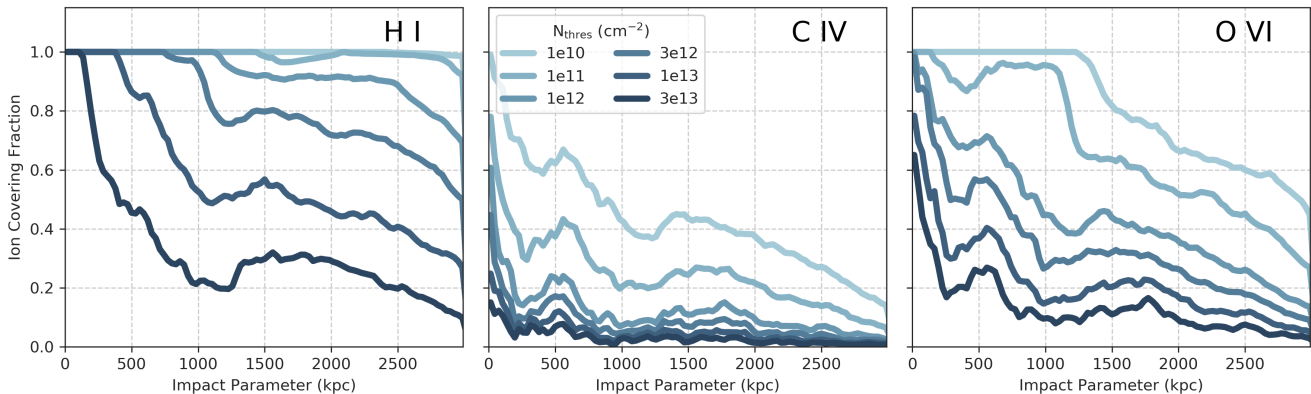


Figure 3. The covering fraction of H I (left panel), C IV (middle panel), and O VI (right panel) as a function of the impact parameter measured from the cluster center at $z = 0.31$. Each line represents the covering fraction for different observational column density thresholds. With existing observational thresholds of *HST/COS* (10^{13} cm^{-2} for H I, $10^{13.1} \text{ cm}^{-2}$ for C IV and $10^{13.3} \text{ cm}^{-2}$ for O VI), we can expect covering fractions above 0.5 and 0.15 for H I and O VI respectively within 1.5 Mpc of the cluster center. At existing observational column density sensitivities, the expected covering fraction for C IV, is below 0.1. Improving the observational threshold by an order of magnitude would result in roughly a 2x increase in the covering fraction of H I and O VI.

perature, density, and metallicity, using an extensive pre-tabulated look-up table generated by CLOUDY (Ferland et al. 2013). The photoionization is calculated assuming an extragalactic UV background described in Haardt & Madau (2012). Using this method, we can determine the mass and number density of any ion throughout the simulation.

We note that we do not explicitly include photoionization from local sources (such as nearby galaxies or AGN). This could produce a significant variation in the photoionization and can have a large impact on ion abundances (Oppenheimer et al. 2018). The uncertainty in the assumed UV background is the largest source of uncertainty in the relative ionic abundances that we derive. For a detailed account of the impact of a varying UVB slope on ion abundances, see the appendix of Werk et al. (2014).

To compute column density profiles, we first generate column density projections centered on the cluster (or individual cluster galaxy) along each axis. From these projections, we gather the distribution of column densities as a function of impact parameter. To convert these column density profiles to covering fractions, we count the fraction of “sightlines” in each radial bin that is above some threshold column density. The existing column density thresholds of *HST-COS* are 10^{13} , $10^{13.1}$, $10^{13.3} \text{ cm}^{-2}$ for H I, C IV, and O VI respectively.

We also use TRIDENT to generate synthetic spectra, allowing for direct comparison with existing observations. To generate a spectrum, we first designate an arbitrary sightline through the simulation volume, analogous to probing a foreground galaxy along the line-of-sight to a QSO. The sightline, l , connects points a and b in a simulation such that $\vec{l} = \vec{r}_b - \vec{r}_a \sum_{i=0}^n d\vec{l}_i$. The length of vector element, $d\vec{l}$ is set by the resolution of the simulation. Absorption features are calculated based on the species’ abundance and gas properties at each vector element. To make the synthetic spectra

more similar to realistic spectra, TRIDENT adds instrument-specific line-spread functions, a Milky Way foreground, a background QSO spectrum, and variable signal-to-noise ratio (S/N). For the analysis presented in §5, we extract synthetic spectra using the *HST/COS* line-spread function (Ghavamian et al. 2009), wavelength coverage of the COS G130M and G160M gratings (approximately 1150-1800Å), no Milky Way foreground absorption, and S/N = 10. These choices are motivated by the feasibility with which our theoretical predictions may be observationally constrained (see discussion in §6).

3 MULTIPHASE ICM PROPERTIES IN THE ROMULUSC SIMULATION

3.1 Evidence for the multiphase ICM

We first demonstrate that the ICM in our simulation is, in fact, multiphase: that gas clouds spanning orders of magnitude in temperature and density exist co-spatially. The high resolution of ROMULUSC is well-suited for resolving the multiphase ICM. With higher resolution (more particles per volume) each spatial region in the simulation is represented with a wider distribution of temperatures and densities, so that the gas is more accurately divided into varying thermodynamic phases (Hummels et al. 2018).

Figure 1 captures the state of the ROMULUSC cluster at $z = 0.31$. The top row highlights properties that are directly measured from simulations but can only be inferred from observations: the density, temperature, and metallicity. The density projection highlights the physical structure of the cluster filled with numerous satellite galaxies. The most massive halo is at the center of the projection frame, surrounded by the hottest and densest regions of the ICM. This cluster is about to undergo a major merger with another galaxy group, which is approaching from the right. Dense filaments trace galaxies flowing through the medium

of Hydrogen and any element, X, Z is the metallicity, and the subscript \odot indicates the solar ratio

as well as gas being stripped from these galaxies through ram-pressure stripping.

The temperature profile is dominated by hot gas at the center of the cluster, reaching ambient temperatures above 10^7 K. Although rare near the cluster center, filaments of warm gas are visible just outside of the virial radius (also see Figure 2). These gaseous filaments are likely a combination of heated cool gas inflows and stripped material from infalling galaxies.

The projected metallicity in the top-right panel demonstrates the extent to which the ICM is enriched with heavy elements. The ambient ICM near the cluster center has a density-weighted average metallicity around $0.3Z_{\odot}$, roughly consistent with values inferred from X-ray observations (Urban et al. 2017). However, the metallicity distribution is far from uniform. At the cluster outskirts, the projected metallicity spans several orders of magnitude (see Figures 4 and 5 for more quantitative analyses of the distribution of metals). The high-metallicity regions trace infalling cluster galaxies, and these structures are easily observable in H I and O VI (see bottom row). The low-metallicity regions show the more pristine ICM, which is difficult to observe with both X-ray emission and UV absorption. The metallicity distribution gradually becomes less clumpy towards the center of the ICM, where gas has had more time to mix. Understanding this distribution of metals throughout the cluster constrains the motion of galaxies through the ICM and the mechanism through which they lose gas.

While the density, temperature, and metallicity are readily available from the simulation data, these properties cannot be measured directly using observations. Rather, these properties must be inferred through careful modeling, which itself depends on various assumptions and model parameters. For this reason, we also show the “observable” cluster properties in the bottom row of Figure 1. The left panel shows the expected X-ray intensity in the 0.5–7.0 keV band and the subsequent middle and right panels show the O VI and H I column densities, respectively. The limits on the colorbars are chosen such that the black background roughly indicates the observational limits of existing instruments, such as *Chandra*, *XMM-Newton* and *HST/COS* (for sensitivities typically obtained, e.g., COS-Halos; Tumlinson et al. 2011).

The gaseous structure observed with X-rays traces the hot, dense gas of the ICM. In contrast, the regions traced through UV absorption comprise the cool-warm phases of the CGM. Warm gas, traced by the O VI column density (bottom row, middle panel), exists as a combination of a volume-filling halo gas and denser gas associated with galaxies. The volume-filling warm gas produces O VI column densities around 10^{13}cm^{-2} in halos of cluster galaxies, especially at the cluster outskirts. Near the centers of gas-rich cluster galaxies, the O VI column density consistently exceeds 10^{16}cm^{-2} . Galaxies moving through the ICM at sufficiently high velocities are stripped of their gas due to ram-pressure forces. Several galaxies in Figure 1 are oriented so that their gas-stripped tails are bright in O VI.

The cool gas, traced by the column density of H I (bottom panel), paints a similar picture for the multiphase structure in the ICM. Compared to the warm gas, the cool gas is more concentrated in galactic centers, and the stripped gas tails of infalling galaxies appear narrower. In certain cases,

the H I shows small-scale, dense structure that is washed out in the distribution of O VI. The diffuse cool gas survives in abundance, both near the cluster center and well beyond its virial radius. The overall similarity in the structures traced by both the warm and cool gas demonstrates the existence of a multiphase medium.

3.2 Radial distribution of the multiphase ICM

We now quantify the mass distribution of the multiphase gas in the cluster at $z = 0.31$. Figure 2 shows the mass fraction of cold, cool, warm, and hot gas as a function of distance from the cluster center.

As expected, hot gas dominates ($> 90\%$ of the mass) in the inner cluster regions. At $r = 2.5R_{200}$ from the cluster center, there is an equal amount of mass in the hot phase and the combined cold, cool, and warm gas phases. At $r = 3R_{200}$ from the cluster center, the warm gas comprises $\sim 45\%$ of the total gas mass while the hot and cool gas phases each comprise $\sim 35\%$ and $\sim 15\%$ of the gas mass, respectively. At these radii, roughly 80% of the gas mass is in the cool-warm phase that could potentially be probed by UV observations. Even at the cluster outskirts, cold gas takes up less than 10% of the total gas mass. Although we don’t expect the mass fraction of cold gas to be higher than the cool or warm phases, the fraction of cold gas in our simulation may be lowered by limitations in resolution. For example, because the simulation cannot resolve very dense regions of very cold gas, the density and temperature thresholds for star formation are relatively low and high, respectively in ROMULUSC.

These results are broadly consistent with the gas mass fractions in the Virgo-sized cluster simulation presented by Emerick et al. (2015). Both simulations predict that hot gas dominates in the inner ICM, that the temperature profile gradually drops with distance from the cluster, and that the cluster outskirts have substantial reservoirs of cool-warm gas. The greatest difference is that our simulations predict a larger fraction of cool and warm gas at the cluster outskirts.

3.3 Covering fraction

The presence of gas in the $T < 10^6$ K temperature regime manifests in observable spectral signatures, namely absorption lines of H I and metal ions. A fundamental metric of any absorption-line survey is the covering fraction, or detection rate, of a given species, defined as the number of sightlines in which that species is observed with some column density (or equivalent width) above a given threshold. To provide a quantitative measure against which our simulation may be tested, we make predictions for the covering fractions of H I C IV, and O VI absorption given a number of detection thresholds throughout the cluster. These three ions span the temperature range of the cool-warm gas phases and have strong UV transitions observable with *HST/COS* at low redshifts. With the medium-resolution *FUV COS* gratings, G130M and G160M, the H I Ly α line is observable at $z \lesssim 0.5$, while the O VI doublet ($\lambda \lambda 1031.9, 1037.6 \text{ \AA}$) shifts into the sensitive wavelength regime of HST at $z \gtrsim 0.11$. The C IV doublet ($\lambda \lambda 1548.2, 1550.8 \text{ \AA}$) is observable down to $z = 0$ but exits the G160M bandpass at $z > 0.16$.

Figure 3 shows the covering fractions of H I, C IV, and

O VI as a function of impact parameter measured from the cluster center. The curves are colored according to various column density thresholds, inevitably showing higher covering fractions for more sensitive thresholds. The darker curves correspond to stronger absorption features, which may be more easily detected in data with lower signal-to-noise ratios (S/N). As we discuss in more detail in §6, S/N ~ 10 spectra are typical for COS, which correspond roughly to 3σ detection limits of 10^{13} cm^{-2} for H I and $3 \times 10^{13} \text{ cm}^{-2}$ for C IV and O VI.

Although the covering fractions of all ions decline with impact parameter, the H I covering fraction declines more slowly than the covering fractions of O VI and C IV. The gas density, temperature, and metallicity all impact the resulting ion abundances, and the various ion tracers constrain the physical conditions of the gas. With the nominal column density limits quoted above, one should detect H I in a majority of sightlines within 1.5 Mpc of the cluster center, O VI in $\sim 15\%$ of sightlines, and C IV in $< 10\%$. O VI has an ionization potential (114 eV) that is more than double that of C IV (48 eV), and it is likely that even the warm ($T > 10^5 \text{ K}$) gas present in the ICM is too hot for carbon to survive in this ionization state; C IV peaks under collisional ionization at $\sim 10^{5.1} \text{ K}$ (Gnat & Sternberg 2007). We measured the statistics for other, lower ionization species observable with COS, such as C III and Si III, showed similarly small covering fractions. Interestingly, the covering fractions suggest that it is possible to detect the presence of warm and cool gas even at the cluster center. Increasing the column density sensitivity by an order of magnitude would approximately double the expected covering fractions throughout the ICM, and we discuss prospects for increased sensitivity in §6.

In a survey using several sightlines probing the Virgo cluster, Yoon et al. (2012) report an increase in H I Ly α covering fraction between $< 1.5 \text{ Mpc}$ ($0.60^{+0.16}_{-0.13}$) and $> 1.5 \text{ Mpc}$ ($1.00_{-0.14}$) for absorbers with $N(\text{H I}) > 10^{13.3} \text{ cm}^{-2}$ and a covering fraction of unity for $N(\text{H I}) > 10^{13.1} \text{ cm}^{-2}$ absorbers. Yoon et al. (2012) attribute this to substructure within Virgo and on its outskirts. Yoon & Putman (2017) conducted a similar study on the Coma Cluster and found a similar covering fraction, albeit without such a difference between inner and outer radii. In a sample of X-ray bright clusters, Burchett et al. (2018) detected H I absorbers in 4/5 clusters. In addition, their data show a hint of increased absorption in the cluster outskirts. Muzahid et al. (2017) detected very strong H I absorbers on the outskirts of three SZ-selected clusters at $R > 1.6R_{500}$, although at higher redshift ($z > 0.4$). Various factors such as cluster dynamical state, redshift, and mass may indeed impact the presence of these absorption-line indicators, but greater amounts of cool gas may reside in the cluster outskirts than our simulations indicate.

3.4 Distribution of metals

As stated above, the diverse range of ICM structures probed by UV absorption should detect gas with different metallicities than the gas typically observed through X-ray emission. Figure 4 shows the distribution of gas temperature and density around $3R_{200}$ around the cluster center. The pixels are colored by the mass-weighted average metallicity of the gas

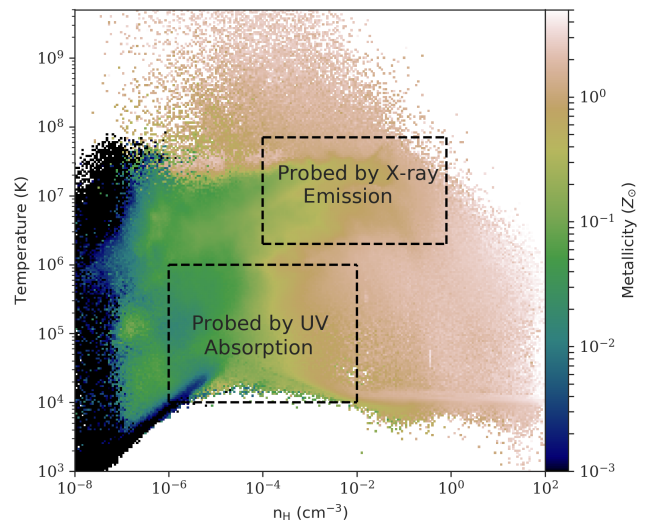


Figure 4. The distribution of the mass-weighted, average metallicity as a function of the temperature and hydrogen number density of the gas. The plot data was taken from a snapshot of RomulusC at $z = 0.31$, within $3R_{200}$ of the cluster center. Gas probed by X-rays exists in a disjoint temperature and density phase from gas probed by UV-lines. The metallicity inferred from X-ray observations is likely to be higher and more uniform than the metallicity probed by UV lines.

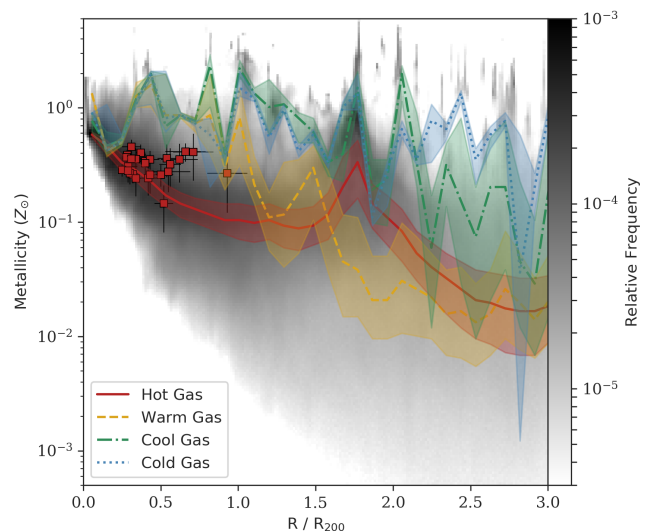


Figure 5. The 3D radial profiles of the median metallicity in cold ($T < 10^4 \text{ K}$), cool ($10^4 < T < 10^5 \text{ K}$), warm ($10^5 < T < 10^6 \text{ K}$), and hot ($T < 10^6 \text{ K}$) gas phases at $z = 0.31$. The shaded regions represent the 68.8% confidence intervals. The gray pixels in the background show the normalized mass distribution of all of the particles in the simulation within $3R_{200}$ of the cluster center. The red squares denote the X-ray derived metallicities from Urban et al. (2017).

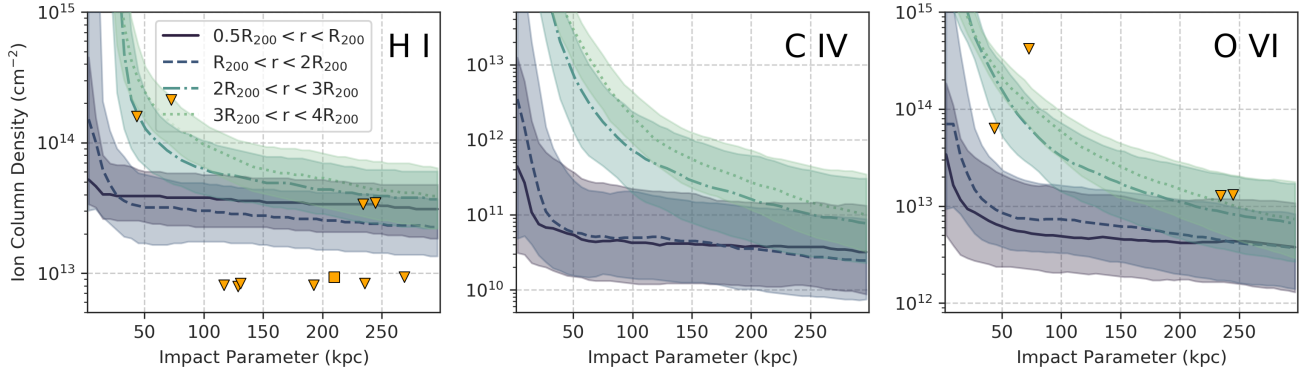


Figure 6. *Left to right:* The column density of H I, C IV, and O VI as a function of impact parameter for all galaxies with stellar masses $M_* > 10^9 M_\odot$ within $4 R_{200}$ of the cluster center. The lines plot the median column density profiles of galaxies within certain bins of distance from the cluster center as indicated in the legend. The shaded regions indicate the 68.8% confidence interval of the distribution. The orange shapes show the observed detections (square) and upper limits (triangles) of H I and O VI in cluster galaxies from [Burchett et al. \(2018\)](#).

that lies in each temperature-density bin. The black square boxes roughly outline the density and temperature ranges that are probed by X-ray and UV observations.

The metallicity of gas probed by X-rays is roughly uniformly $0.3Z_\odot$ with a small dispersion. At the high temperature end ($T > 3 \times 10^7 \text{K}$), the average metallicity of the gas is consistently above solar metallicity. This is likely dominated by hot, dense, and metal-rich supernova or AGN ejecta throughout the simulation. In contrast, the low-density region at lower temperatures exhibits lower metallicities, likely tracing the diffuse cluster outskirts that are, on average, less polluted with metals than the ICM near the cluster center (see Figure 1). Overall, the bulk of the metals traced by X-ray observations belong to the hot, dense ICM. The X-ray emission is strongest near the cluster center, where the metals have been thoroughly mixed in the turbulent ICM.

Gas traced by the UV has a significantly larger variation in its average metallicity. In this regime, the metallicity is also a tracer of the gas density. Intuitively, this wide range in metallicity traces gas being stripped from galaxies within and around the cluster. For example, in Figure 1, the filamentary structures in the projected metallicity often trace the filamentary structures in the temperature and density. The ISM and CGM of galaxies are stripped of their high-metallicity gas as they move through the ICM. Over time, these metals mix with the ambient ICM. With the sensitivity to a much wider range in densities, UV observations can better measure the inhomogeneity of ICM the metallicity.

In Figure 5, we further quantify the distribution of metals in each of the different gas phases (red, orange, green, and blue for hot, warm, cool and cold, respectively) by plotting the median metallicity profiles of each temperature phase. The shaded areas show the 68.8% confidence interval of each gas distribution. The grey pixels show the normalized distribution of all gas (without temperature cuts) within 3 Mpc of the cluster center. The red squares show X-ray measured metallicities from [Urban et al. \(2017\)](#).

This radial metallicity profile highlights the range of metallicities in the multiphase gas predicted in Figure 4. For

example, consider the inner Mpc around the cluster center, which is composed of mostly hot gas (see Figure 2). Although the observed metallicities are roughly constant at $0.3Z_\odot$, our simulation predicts that the spread in metallicities (considering all phases) spans significantly more than an order of magnitude. This spread is even larger at the cluster outskirts, reflecting the mixture of multiphase gas comprising the ISM, CGM and ICM with a wide range of temperatures and metallicities.

Furthermore, the different gas phases have varied metallicity profiles. The median metallicity of the hot gas phase is highest at the cluster center and decreases with radius. Although there is still a substantial mass of hot gas at the cluster outskirts, the metals from stripped CGM are not as well mixed as that near the cluster center. We predict that (by mass) the median metallicity of hot gas beyond $0.5 R_{200}$ is actually below that reflected by X-ray observations. The metallicity profiles of the cool and cold phases have higher median metallicity values than the hot phase at nearly all radii, because of the metal-rich gas in the cool CGM and ISM of galaxies within the cluster. However, the metallicity profile of the warm gas falls off more rapidly than that of the cool or cold gas, and the warm gas metallicity is more representative of the global median at $> 1.5 R_{200}$. Also beyond $1.5 R_{200}$, the median profiles of the cool and cold gas show large variations due to the stochasticity in the distribution of galaxies and thus track relatively well with the infalling galaxies' CGM metal contents.

While the lack of metals present beyond $0.5R_{200}$ may indicate that ROMULUSC fails to transport metals as effectively as it should, we stress that these results are sensitive to the redshift at which we sample the simulation. At redshifts more consistent with observations ($z < 0.2$), the cluster outskirts are more metal-enriched. For the sake of consistency, we limit our analysis to $z = 0.31$ and will explore the time evolution of the ICM in future work. We also stress that no attempt was made to mimic X-ray observations beyond selecting for hot gas. As X-ray observations are more sensitive

to denser gas, they may be biased toward higher metallicity relative to the median presented in Figure 5.

4 THE CGM OF ROMULUSC CLUSTER GALAXIES

The hot and dense ICM plays an important role in the evolution of cluster galaxies. For example, galaxies moving through the ICM often experience strong ram-pressure forces that strip them of their gas and quench star formation. Although this effect appears in many modern simulations (e.g. Bahé et al. 2017; Zinger et al. 2018; Tremmel et al. 2019), the quenching timescales differ depending on whether the ISM is stripped directly or indirectly deprived of replenishing fuel from a CGM that has been stripped early upon infall. We explore the effects of the cluster environment upon the observable ion abundances in sightlines probing the CGM of cluster galaxies at various radii.

In Figure 6, we compare the ion column densities of H I, C IV, and O VI as a function of impact parameter measured from the centers of cluster-galaxy halos. Each line shows the median column density for all galaxies with stellar masses of $M_* > 10^9 M_\odot$ within the bins of projected distance from the cluster center indicated in the legend. Each shaded regions contain the 68% confidence interval of the distribution in each radial bin. The orange markers show the observed detections (square) and upper limits (triangle) of H I and O VI in cluster galaxies from Burchett et al. (2018). Although C IV does not have comparable observations, we include its column density profile as this ion is observable with HST/COS at the lowest redshifts. Note that we do not include predictions for galaxies within $0.5R_{200}$. We find that, in this regime, the ‘detected’ ions (especially H I) are dominated by the ambient ICM and are not necessarily signatures of the CGM of individual galaxies.

Our simulation predictions are broadly consistent with the limited existing CGM O VI observations. However, the H I column densities we predict at impact parameters > 100 kpc generally exceed the observational data. A preliminary check of lower-redshift ($z = 0.1, 0.2$) simulation snapshots show lower H I CGM column densities more consistent with the observations but that are still high. We will explore this redshift evolution further in future work. Nevertheless, this inconsistency may also reflect some aspect of the galaxy-CGM-ICM interaction that is not accurately reproduced by our simulation. Larger samples of observational data will prove invaluable to constraining the simulated physics.

Notably, we predict a decrease in CGM column densities at impact parameters $\lesssim 200$ kpc for galaxies with projected clustocentric distances of $< 2R_{200}$. Below distances of $2R_{200}$ there is little evolution of the column density profiles beyond the very innermost ($\lesssim 25$ kpc) impact parameters. The larger clustocentric bins show progressively decreasing profiles from $> 3R_{200}$ to $2 < r/R_{200} < 3$ before the more dramatic decline at $2R_{200}$. Thus, the majority of the CGM is stripped while galaxies are still quite far from the cluster center; however, the innermost CGM requires much greater ram pressure to become stripped, as it is the most bound. It is interesting to note that, at large impact parameters, the column densities we predict for O VI are lower than many of the observations from the COS-Halos isolated galaxy sample

(Tumlinson et al. 2013). Simulations of isolated galaxies using the same sub-grid physics models as ROMULUSC recover the COS-Halos O VI column densities quite well (Sanchez et al. 2018), indicating that the cluster environment is inducing strong effects on the CGM of galaxies even out to clustocentric distances of $4R_{200}$. We defer a more in-depth comparison between simulated cluster and isolated galaxies as well as observations thereof to a future work.

In Figure 7, we show the covering fractions of H I, C IV, and O VI as a function of impact parameter for the same galaxies considered in Figure 6. Each line represents the combined covering fraction of all galaxies within each distance bin calculated for the observationally motivated column density thresholds of 10^{13} , $10^{13.1}$, and $10^{13.3} \text{ cm}^{-2}$ for H I, C IV, and O VI, respectively. The covering fraction of C IV is low at large impact parameters even for galaxies in the outskirts of the cluster. At smaller impact parameters, C IV becomes depleted for galaxies within $2R_{200}$ from the cluster center. A similar effect is seen for O VI, although the covering fraction is generally higher than that of C IV at all impact parameters and the profile steepens significantly within $2R_{200}$. The covering fractions of H I decline very modestly with impact parameter, and the evolution with clustocentric distance is much greater for the metal ion diagnostics O VI and C IV. As a general trend, galaxies farther from the cluster center tend to retain more of their CGM, resulting in higher covering fractions of C IV and O VI; ram-pressure increases closer to the cluster center where the density of the ICM is higher.

5 THE PHYSICAL CONDITIONS OF COOL AND WARM GAS IN THE ICM FROM SYNTHETIC SPECTRA

Herein, we discuss several facets of a multiphase ICM, which in turn have observable signatures, particularly in the UV regime for $T < 10^6 \text{ K}$ gas. In this subsection, we seek to 1) further assess the observability of this material and 2) relate the observable signatures back to the physical conditions of the gas in the ROMULUSC simulation. Our intent is to provide a proof-of-concept level of analysis while sampling various regions throughout the cluster, as would be probed in an actual absorption-line spectroscopic survey using sightlines piercing galaxy clusters.

Using Trident (Hummels et al. 2017, discussed in §2.2), we extracted sixteen sightlines through the ROMULUSC cluster; the sightline locations are indicated in Figure 8. The sightlines were chosen to pass through ambient ICM regions far away from infalling galaxies, the immediate CGM of cluster galaxies, and detritus stripped as galaxies fall into the cluster. The virial radii of subhalos within the cluster are marked with circles in Figure 8. We then analyzed the resulting synthetic spectra as an observer might analyze such data probing an actual cluster obtained with HST/COS, the only currently available instrument that is capable of producing a similar dataset (see discussion in §6).

Three examples of spectra we extracted are shown in Figure 10; in each plot, the individual panels show the would-be locations of H I Ly α and Ly β , the O VI λ 1031, 1037Å doublet, and C III λ 977Å within 2000 km/s of the cluster redshift. For each spectrum, we searched by-eye for

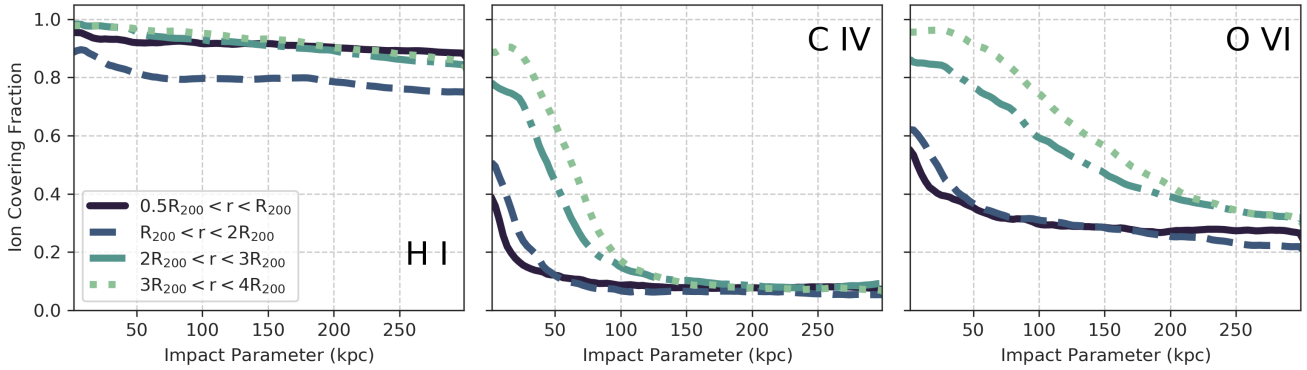


Figure 7. The covering fractions of H I, C IV, and O VI as a function of halo-centric impact parameter for all galaxies with $M_* > 10^9 M_\odot$ at $z = 0.31$. The different lines represent halos within the indicated distance bins from the cluster center. Covering fractions measure the fraction column densities above some threshold column density. We assume column density thresholds of 10^{13} cm^{-2} for H I, $10^{13.1} \text{ cm}^{-2}$ for C IV, and $10^{13.3} \text{ cm}^{-2}$ for O VI. The covering fraction of all ions is lower for galaxies nearer to the cluster center.

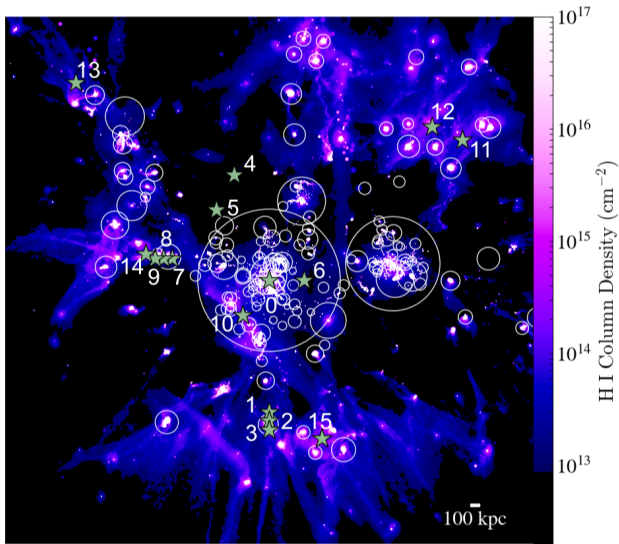


Figure 8. The O VI column density overplotted with locations of sightlines for which we extracted synthetic spectra. The virial radii of cluster galaxies with stellar masses of $M_* > 10^9 M_\odot$ are indicated by circles (centered on each galaxy).

absorption signatures of these four lines, marking the approximate velocity of each component. In total, we visually identified 20 components of H I, O VI, or C III in our synthetic spectra sample.

Two key factors hinder detecting weaker lines: the S/N of the data and line broadening due to thermal and non-thermal motions. Thus, the wavelength coverage of multiple transitions enables one to corroborate identifications of features using the presence of other lines. For example, a strong Ly α line should be accompanied by a weaker (the ratio set by atomic physics) Ly β line at the same velocity. Similarly, albeit with caution, one can corroborate lines of one species (e.g., O VI) with absorption by another (e.g., H I). While this practice can lead to misidentifications if applied improperly,

it is occasionally necessary in cases with weak features or blending due to lines from other redshifts. Our dataset analyzed here (and as would be analyzed from an actual survey) presents a number of such challenges, as the special cluster environment contains an excess of hotter gas relative to random CGM/IGM regions; the increased gas temperature thermally broadens H I lines substantially.

We highlight one particularly illustrative case that underscores the importance of wavelength coverage in this analysis, shown in the middle panel of Figure 10 at $v \sim -250$ km/s. While no Ly β is detected, a broad Ly α feature is barely apparent. However, the O VI doublet is well detected at this velocity, greatly reinforcing the broad Ly α identification. The width of the Ly α line then enables a direct constraint on the gas temperature. Furthermore, without the Ly α coverage, one may identify the O VI doublet as a spurious superposition of two Ly α lines at lower redshifts. While the O VI and Ly β lines would be covered in a COS observation with only the G130M grating, observations with the G160M would be required to cover the observed wavelength of Ly α . The symbiotic complementarity of information gleaned from both gratings is essential to both discovering this gas system and understanding its physical conditions.

Upon identifying the absorption features in the synthetic spectra, we fitted Voigt profiles to each feature using the *Veeper* software originally developed for the analysis of Burchett et al. (2015). Measurements for all detected H I and O VI lines as well as information about their respective sightlines are provided in Table 1. Notably, we detect several broad Ly α lines, with seven components having Doppler parameter values $b > 40$ km/s, tracing warm gas at $T > 10^5$ K (assuming thermal broadening). To compare this synthetic sample with previous survey measurements of broad Ly α absorbers, we perform an approximate conversion of absorber line density as measured through our simulation to the line density metric often reported in absorption-line surveys dN/dz , or number of absorbers per unit redshift. Our sightlines extend 5 Mpc through the ROMULUSC simulation, which corresponds to the luminosity distance difference over $\Delta z \sim 0.0008$ at $z = 0.31$ (assuming cosmological parameters

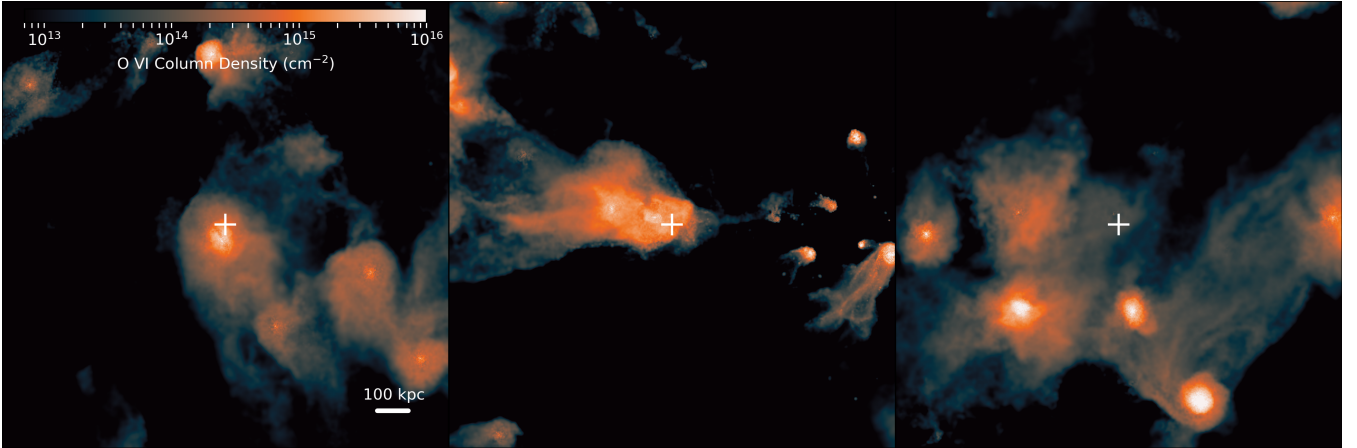


Figure 9. The H I column density around the regions of the sightlines presented in Figure 10. Each sightline was chosen at an arbitrary location, in-between galaxies at the $z = 0.31$ snapshot of ROMULUSC. It is not required that a sightline directly intersect the CGM of a galaxy for there to be detectable amounts of O VI in the ICM.

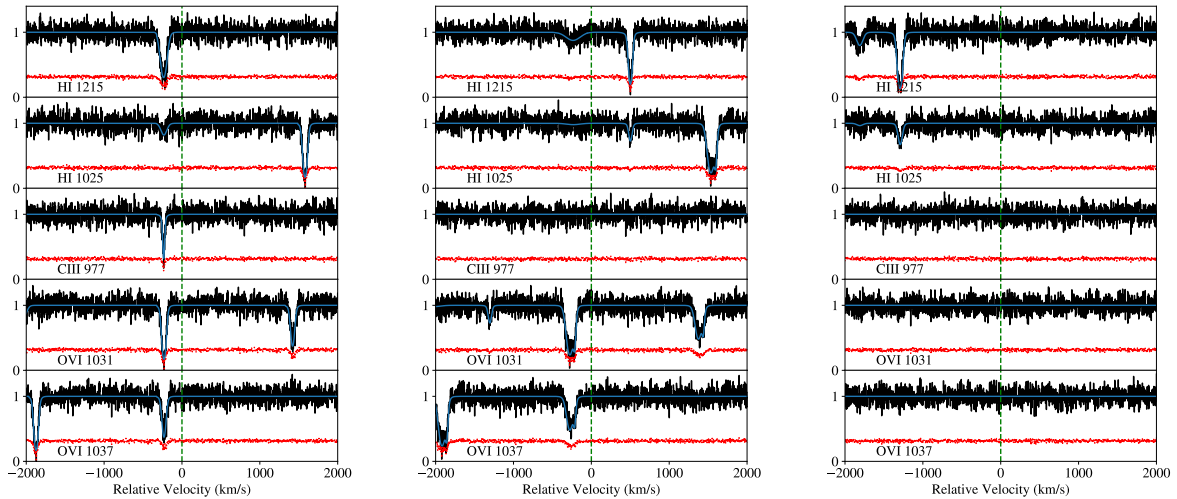


Figure 10. Synthetic spectra of sightlines generated using TRIDENT through the ROMULUSC cluster. From left to right, the panels correspond to Sightlines 2, 7, and 12 marked in Figure 9. Each subpanel shows absorption (or lack thereof) for the transition labelled in its lower right corner, relative to $z = 0.31$. The blue curves mark Voigt profile fits to the visually identified absorption components. Note that the apparent absorption at > 1000 and < 1000 km/s in the Sightline 2 and 7 H I 1025, O VI 1031, and O VI 1038 panels are actually O VI 1031, O VI 1037, and O VI 1031 lines, respectively, due to the large velocity range plotted. These spectra show the diversity of absorbers predicted by our simulation, including broad and narrow H I components with and without corresponding O VI and C III.

from Planck Collaboration et al. (2016)). Thus, over the 16 sightlines we have analyzed, our broad Ly α density would translate to $dN/dz \sim 540$. Compared with the broad Ly α $dN/dz \sim 25$ from Lehner et al. (2007), our broad Ly α sample represents a $> 20x$ overdensity relative to random IGM sightlines. Of course, our measurement is heavily biased, as all of our sightlines fall within the cluster environment, and the incidence of broad Ly α absorbers should increase in such overdense regions (e.g., Tepper-García et al. 2012). Perhaps a more fair comparison is with the survey by Tejos et al. (2016), who examined the line density near putative intracluster filaments and find a broad Ly α $dN/dz = 108^{+65}_{-43}$

within 3 Mpc of such filaments. We again emphasize that these comparisons are by no means rigorous, as we furthermore did not choose our sightline locations at random locations throughout the cluster, and the pathlength calculation (denominator of these metric) requires accounting for the sensitivity limits of the spectra, etc. However, our predictions indicate that a substantial number of broad Ly α absorbers tracing warm gas, well in excess of the typical IGM or even Cosmic Web filaments, should await discovery within the cluster environment.

Table 1. Voigt profile fitting results for identified absorption components in

Sightline ^a	Ion	$\log(N/\text{cm}^{-2})$	b [km/s]	v^b [km/s]	ρ_{cl}^c [kpc]	$\log(T/\text{K})^d$	$\log(N_H/\text{cm}^{-3})$
0	H I	17.25 ± 0.30	15 ± 1	-357.7 ± 1.1	0	7.10	-1.88
0	H I	16.70 ± 0.99	20 ± 4	-170.0 ± 1.8	0	7.10	-1.88
2	O VI	14.55 ± 0.04	28 ± 3	-233.6 ± 1.8	1600	6.27	-4.65
2	H I	13.94 ± 0.04	47 ± 5	-234.8 ± 3.4	1600	6.27	-4.65
3	O VI	14.13 ± 0.06	36 ± 7	-258.7 ± 4.4	1700	6.15	-4.84
3	H I	13.62 ± 0.09	61 ± 17	-264.2 ± 10.5	1700	6.15	-4.84
7	O VI	14.03 ± 0.19	16 ± 8	-216.3 ± 4.0	1128	6.49	-4.34
7	O VI	14.59 ± 0.06	49 ± 8	-277.9 ± 6.9	1128	6.49	-4.34
7	H I	13.92 ± 0.05	24 ± 3	500.4 ± 2.2	1128	6.49	-4.34
7	H I	13.35 ± 0.16	121 ± 55	-233.9 ± 36.7	1128	6.49	-4.34
8	H I	17.40 ± 0.23	18 ± 1	-299.2 ± 1.2	1226	6.45	-4.47
8	O VI	14.64 ± 0.04	27 ± 2	-326.4 ± 1.6	1226	6.45	-4.47
9	H I	13.54 ± 0.10	49 ± 17	-279.8 ± 10.7	1324	6.40	-4.91
9	O VI	14.46 ± 0.04	25 ± 3	-284.3 ± 1.9	1324	6.40	-4.91
10	H I	13.26 ± 0.11	27 ± 10	-534.7 ± 6.7	500	6.73	-4.26
11	H I	13.23 ± 0.13	42 ± 17	-1310.8 ± 11.6	2720	5.43	-5.38
12	H I	14.11 ± 0.04	32 ± 3	-1293.5 ± 2.0	2547	5.49	-5.31
12	H I	13.23 ± 0.14	50 ± 22	-1810.2 ± 14.7	2547	5.49	-5.31
15	H I	13.55 ± 0.08	69 ± 16	-1092.0 ± 10.9	1897	5.79	-5.34

^a Sightline numbers correspond to those marked in Figure 8.^b Velocities are expressed relative to the RomulusC snapshot redshift at $z = 0.31$.^c Impact parameter of sightline relative to the cluster center^d Quantity averaged along sightline

6 PROSPECTS OF STUDYING THE COOL AND WARM GAS IN GALAXY CLUSTERS

We now turn to using the results from our simulation to observationally constrain the multiphase ICM and the CGM of cluster galaxies. In §3 we show that a substantial fraction of the ICM is composed of cool and warm gas beyond $1.5 R_{200}$. This gas can be traced observationally through H I, O VI, and (to a lesser extent) C IV. In §3.3 and §4 we predict the covering fractions of these three ions as a function of both clustocentric and halo-centric impact parameters. Here, we further examine the feasibility of observing the cool and warm cluster gas with existing and future UV telescopes.

The predicted covering fractions depend on both the physical abundance of the ion and the column density sensitivity limits of the observing instrument. In our calculations, we assume constant column density sensitivities of *HST/COS* set by the anticipated S/N of the spectra. However, in practice, the sensitivity limits depend on several different factors, and a given S/N does not directly map onto one sensitivity limit. For example, warm gas will produce more thermal broadening than cool gas, which will result in shallower absorption features and a higher minimum observable column density even with the same S/N. Furthermore, stochastic noise can make some otherwise detectable lines insignificant. Instead, the more reliable metric for determining the column density sensitivity of an instrument is the detection significance. The detection significance uses the S/N, column density, temperature (assuming thermal broadening), and the instrument-specific line-spread function to measure the ratio of the line width and its uncertainty, W/σ_W . Lines with a detection significance $\geq 3\sigma$ are considered to be detectable. We refer the reader to Burchett et al. (2018) for a detailed description of this calculation.

Figure 11 uses the detection significance described above to show the minimum observable column density of H I and O VI as a function of temperature for several different S/N. The dotted horizontal lines indicate the average covering fractions of H I and O VI within $R < 2$ Mpc of the cluster center at three different column density thresholds (see Figure 3). At each S/N line, the minimum observable column density of H I increases with temperature due to the expected thermal broadening. In contrast, the minimum observable column density of O VI slightly decreases with temperature. This is likely due to the fact that the collisional equilibrium temperature of O VI is $\sim 10^{5.5}$ K. For both ions, increasing the S/N from 10 to 75 improves the column density sensitivity limit by ~ 1 dex.

The S/N of a far-UV spectrum is a function of the brightness of the background source and the integration time. In Figure 12, we show the predicted S/N of LUVOIR as a function of the GALEX FUV magnitude for different exposure times. The horizontal dashed lines show the covering fractions of H I and O VI in ROMULUSC for several different S/N (assuming each S/N corresponds to the median detectable column densities in Figure 11).

Currently, the most sensitive UV spectrograph to H I and O VI at low and intermediate redshifts is the *HST/COS*. It consistently reaches S/N of at least 10, and can reach S/N values as high as 75 (corresponding to the full range of S/N lines in Figure 11). For example, as of the July 2018 data release of the Hubble Spectroscopic Legacy Archive (HSLA; Peebles et al. 2017), 300 sightlines have $S/N \geq 10$, 100 sightlines have $S/N \geq 20$, and 16 sightlines have $S/N \geq 50$. Using the covering fraction estimates presented in Figure 12, we predict that *HST/COS* can detect minimum covering fractions of 0.66 for H I and 0.19 for O VI.

The next-generation UV instruments are still in the concept phase, vying for recommendation by the Astro2020

Decadal Survey. Current examples include The Large Ultraviolet Optical Infrared (*LUVUIR*) observatory (Bolcar et al. 2017), which would feature a 15 meter aperture, as well as a host of instruments spanning the UV to the infrared, such as the Large Ultraviolet Multi-object Spectrograph (LUMOS; Harris et al. 2018). Although facilities of this magnitude would likely not launch until the 2030s, we explore their anticipated advancements of UV cluster observations below, with the goal of understanding the prospect of studying the multiphase ICM in the coming decades.

LUVUIR would dramatically increase the S/N and observable column density limits. For example, achieving the nominal S/N = 10 we have assumed throughout the work requires 5 hours of exposure time with *HST/COS* for a source with $m_{FUV} = 19.5$. Achieving a similar S/N on *LUVUIR* would only take 20 minutes. Furthermore, for modest exposure times of 2-4 hours, *LUVUIR* can deliver $S/N \geq 50$ (corresponding to covering fractions of 0.91 for H I and 0.37 for O VI) for a large fraction of sources. However, according to our predictions, increasing the S/N to ≥ 100 brings marginal returns.

The transformational leap beyond current capabilities will likely come from the ability to observe a larger sample of background sources. At fainter magnitudes ($m_{FUV} > 20$), the density of background sources (e.g., QSOs and star-forming galaxies) in the sky increases sharply (Rubin et al. 2018). For example by cross-matching the UV Ultra Deep Field catalog (Rafelski et al. 2015) with the GALEX UV source catalog (Bianchi et al. 2017) at $z = 0.2 - 1$, we found that there are ≥ 5900 sources per square degree with $m_{FUV} \geq 22$. Considering clustocentric impact parameters within 2 Mpc, this source density translates to ≥ 200 possible sources *per cluster*. Therefore, one could easily subselect the cluster sample based on the properties of the cluster or study a particular cluster in exquisite detail, following a similar approach to that of Yoon et al. (2012) and Yoon & Putman (2017) for Virgo and Coma, respectively, but for *virtually any clusters in the sky*.

7 CONCLUSIONS

We use the high-resolution hydrodynamical galaxy cluster simulation, ROMULUSC, to examine the multiphase structure of the intracluster medium (ICM) and its effect on the circumgalactic media (CGM) of constituent galaxies. We focus our analysis on cool-warm ($T = 10^4 - 6$ K) gas at the cluster outskirts which is particularly difficult to observe in X-rays. We show that this gas can be observed in the ultraviolet (UV) with *HST/COS* and make predictions for observations with next-generation telescopes, like *LUVUIR*. We summarize our key findings as follows:

(i) At all clustocentric radii, we find significant quantities of multiphase gas in the cool ($10^4 - 5$ K) and warm ($10^5 - 6$ K) gas phase, observable in the UV. Relative to the hot ($T > 10^6$ K), X-ray emitting gas, the share of cool-warm material increases rapidly toward the cluster outskirts. By $r > 2.5R_{200}$, the warm gas mass fraction exceeds that of the hot gas, and even the cool gas exceeds the hot gas at $r > 3.5R_{200}$.

(ii) The ICM is marked by a wide range of metallicity from $Z \approx 0.01Z_{\odot}$ to $Z > Z_{\odot}$. Our simulations predict that the

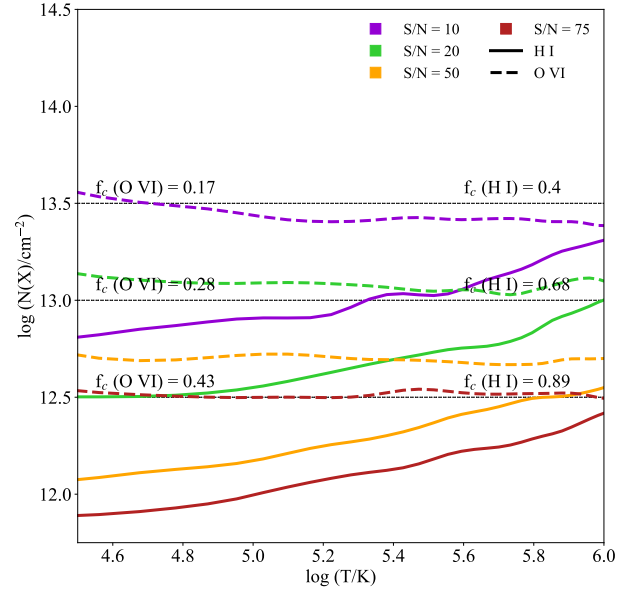


Figure 11. The detectability (at 3σ) of H I Ly α (solid) and O VI λ 1032Å (dashed) lines over a range of column densities and temperatures (via the Doppler b parameter) given several levels of S/N achieved (see color-coding in legend). Mean covering fractions of H I and O VI at three column density thresholds at clustocentric impact parameters $\rho < 2$ Mpc are indicated by horizontal dotted lines. For example, a S/N = 10 spectrum should return a covering fraction $\sim 17\%$ for O VI across the warm temperature regime but $f_c = 50 - 70\%$ for H I across this same temperature range.

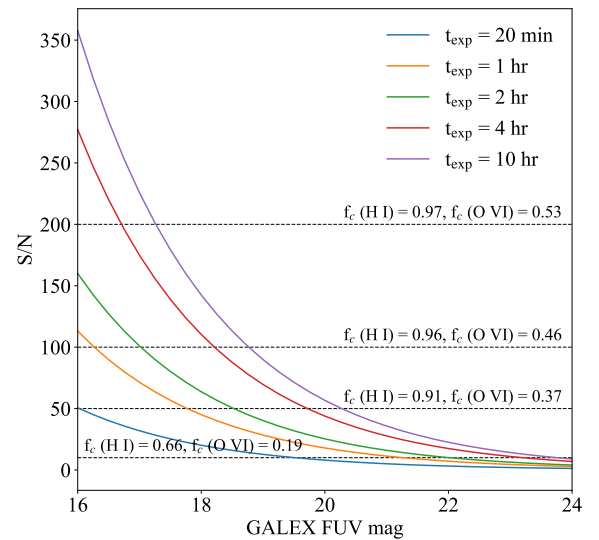


Figure 12. Signal-to-noise (S/N) ratio achieved under the current *LUVUIR* 15m telescope concept when observing UV-bright sources at various exposure times (color coding indicated in legend). The horizontal lines indicate covering fractions of H I and O VI assuming the column densities detectable of each ion at the indicated S/N (see Figure 11).

gas at temperatures and densities probed by X-rays exhibits metallicities broadly consistent with X-ray measurements at $r < R_{200}$; however, the lower temperature and density regime to which the UV is sensitive possesses a much wider range in metallicity, including lower metallicities from the well-mixed ICM and highly enriched gas that is stripped from the CGM of infalling galaxies.

(iii) We predict detection rates of H I, C IV, and O VI which sample different temperatures of the cool-warm gas, throughout the ICM. We find that the detection profiles of all three ions decline from the cluster center out to 1 Mpc, but remain relatively flat out to the edge of the simulated volume, at 3 Mpc.

(iv) The CGM of cluster galaxies are readily stripped during the early stages of infall. CGM stripping is apparent in galaxies as far as $4R_{200}$ from the cluster center and becomes progressively more pronounced near the cluster center. This stripping is observable in the halo-centric covering fractions of H I, C IV, and O VI for galaxies at various distances from the cluster center.

(v) To test the feasibility of confronting our galaxy cluster simulation and the physics therein with observations, we generate and analyze synthetic UV spectra of sightlines piercing the ROMULUS ICM and CGM of cluster galaxies. Within 16 synthetic sightlines, we detect 19 components of H I, O VI, and C III, including several broad Ly α components tracing the elusive warm gas regime, in various environments from the cluster center to the outskirts. These synthetic data demonstrate that a large UV spectroscopic survey using currently available instrumentation can effectively be leveraged to test cluster formation and evolution models.

(vi) Considering current and future UV spectroscopic capabilities, we examine potential observing strategies to constrain the multiphase ICM and cluster galaxy CGM. Substantive, important progress can be made now with *HST/COS* given modest investments of telescope time, for an ensemble of clusters probed by UV-bright ($m_{\text{FUV}} < 19$) QSOs to constrain the cool-warm gas profiles, metal enrichment, and CGM in cluster models. Dramatically improved diagnostic power would be afforded by a large-aperture space-borne UV-sensitive telescope such as the *LUVOIR* concept currently being considered. For the same ensemble of clusters one could observe at $S/N \sim 10$ with *HST/COS*, *LUVOIR* would deliver $S/N = 50 - 100$ and detect extremely diffuse cool-warm gas approaching detection rates of 90%.

UV spectroscopy provides unique insights into the cold-warm gas in and around the most massive structures in the Universe and offers a highly complementary view of the baryonic contents of galaxy clusters derived from X-ray and microwave observations. Together, these forthcoming multi-wavelength observations will provide a comprehensive view of the multiphase gas in the ICM of galaxy clusters and the CGM of cluster galaxies to transform our understanding of galaxy cluster physics and galaxy evolution.

ACKNOWLEDGEMENTS

IB would like to thank Cameron Hummels, Nicole Sanchez, and Akaxia Cruz for their insightful conversations regarding this work. This research is part of the Blue Waters sustained-petascale computing project, which is supported by the Na-

tional Science Foundation (awards OCI-0725070 and ACI-1238993) and the state of Illinois. Blue Waters is a joint effort of the University of Illinois at Urbana-Champaign and its National Center for Supercomputing Applications. This work is also part of a Petascale Computing Resource Allocations allocation support by the National Science Foundation (award number OAC-1613674). This work also used the Extreme Science and Engineering Discovery Environment (XSEDE), which is supported by National Science Foundation grant number ACI-1548562. Resources supporting this work were also provided by the NASA High-End Computing (HEC) Program through the NASA Advanced Supercomputing (NAS) Division at Ames Research Center.

ISB, TQ and MT were partially supported by NSF award AST-1514868. ISB received partial support from NASA award HST-AR-15046. MT gratefully acknowledges support from the YCAA Prize Postdoctoral Fellowship.

REFERENCES

- Allen S. W., Evrard A. E., Mantz A. B., 2011, *ARA&A*, 49, 409
 Asplund M., Grevesse N., Sauval A. J., Scott P., 2009, *ARA&A*, 47, 481
 Bahé Y. M., et al., 2017, *MNRAS*, 470, 4186
 Bianchi L., Shiao B., Thilker D., 2017, *The Astrophysical Journal Supplement Series*, 230, 24
 Bolcar M. R., et al., 2017, in *Society of Photo-Optical Instrumentation Engineers (SPIE) Conference Series*. p. 1039809
 Booth C. M., Schaye J., 2009, *MNRAS*, 398, 53
 Bordoloi R., et al., 2014, *ApJ*, 796, 136
 Burchett J. N., et al., 2015, *ApJ*, 815, 91
 Burchett J. N., Tripp T. M., Wang Q. D., Willmer C. N. A., Bowen D. V., Jenkins E. B., 2018, *MNRAS*, 475, 2067
 Cen R., Ostriker J. P., 1999, *ApJ*, 514, 1
 Davies R. D., Lewis B. M., 1973, *MNRAS*, 165, 231
 Dressler A., 1980, *ApJ*, 236, 351
 Emerick A., Bryan G., Putman M. E., 2015, *MNRAS*, 453, 4051
 Emerick A., Bryan G. L., Mac Low M.-M., 2019, *MNRAS*, 482, 1304
 Ferland G. J., et al., 2013, *Rev. Mexicana Astron. Astrofis.*, 49, 137
 Fraser-McKelvie A., Brown M. J. I., Pimbblet K., Dolley T., Bonne N. J., 2018, *MNRAS*, 474, 1909
 Fumagalli M., Fossati M., Hau G. K. T., Gavazzi G., Bower R., Sun M., Boselli A., 2014, *MNRAS*, 445, 4335
 Ge C., Wang Q. D., Tripp T. M., Li Z., Gu Q., Ji L., 2016, *MNRAS*, 459, 366
 Ghavamian P., et al., 2009, Technical report, Preliminary Characterization of the Post-Launch Line Spread Function of COS
 Gnat O., Sternberg A., 2007, *ApJS*, 168, 213
 Gunn J. E., Gott III J. R., 1972, *ApJ*, 176, 1
 Haardt F., Madau P., 2012, *ApJ*, 746, 125
 Harris W., France K., Fleming B., Bolcar M., 2018, AGU Fall Meeting Abstracts
 Hopkins P. F., et al., 2018, *MNRAS*, 480, 800
 Hummels C. B., Smith B. D., Silvia D. W., 2017, *ApJ*, 847, 59
 Hummels C. B., et al., 2018, arXiv e-prints,
 Jáchym P., Combes F., Cortese L., Sun M., Kenney J. D. P., 2014, *ApJ*, 792, 11
 Johnson S. D., Chen H.-W., Mulchaey J. S., 2015, *MNRAS*, 449, 3263
 Kravtsov A. V., Borgani S., 2012, *ARA&A*, 50, 353
 Lake G., Katz N., Moore B., 1998, *ApJ*, 495, 152
 Lau E. T., Kravtsov A. V., Nagai D., 2009, *ApJ*, 705, 1129

- Lau E. T., Nagai D., Avestruz C., Nelson K., Vikhlinin A., 2015, *ApJ*, **806**, 68
- Lehner N., Savage B. D., Richter P., Sembach K. R., Tripp T. M., Wakker B. P., 2007, *ApJ*, **658**, 680
- Menon L., Wesolowski F., Zheng G., Jetley P., Kale L. V., Quinn T. R., Governato F., 2015, in *Adaptive Techniques for Clustered N-Body Cosmological Simulations*. *Computational Astrophysics and Cosmology*, **2**, 1..
- Mernier F., et al., 2018, *Space Sci. Rev.*, **214**, 129
- Moore B., Katz N., Lake G., Dressler A., Oemler A., 1996, *Nature*, **379**, 613
- Mroczkowski T., et al., 2019, *Space Sci. Rev.*, **215**, 17
- Muzahid S., Charlton J., Nagai D., Schaye J., Srianand R., 2017, *The Astrophysical Journal Letters*, **846**, L8
- Nagai D., Lau E. T., 2011, *ApJ*, **731**, L10
- Nagai D., Lau E. T., Avestruz C., Nelson K., Rudd D. H., 2013, *ApJ*, **777**, 137
- Nelson K., Lau E. T., Nagai D., 2014, *ApJ*, **792**, 25
- Nelson D., et al., 2019, arXiv e-prints,
- Nielsen N. M., Kacprzak G. G., Pointon S. K., Churchill C. W., Murphy M. T., 2018, *ApJ*, **869**, 153
- Oppenheimer B. D., Schaye J., 2013, *MNRAS*, **434**, 1043
- Oppenheimer B. D., Segers M., Schaye J., Richings A. J., Crain R. A., 2018, *MNRAS*, **474**, 4740
- Peeples M., et al., 2017, Technical report, The Hubble Spectroscopic Legacy Archive
- Planck Collaboration et al., 2016, *Astronomy and Astrophysics*, **594**, A13
- Pointon S. K., Nielsen N. M., Kacprzak G. G., Muzahid S., Churchill C. W., Charlton J. C., 2017, *ApJ*, **844**, 23
- Pontzen A., Tremmel M., 2018, *ApJS*, **237**, 23
- Pontzen A., Roškar R., Stinson G. S., Woods R., Reed D. M., Coles J., Quinn T. R., 2013, pynbody: Astrophysics Simulation Analysis for Python
- Pontzen A., Tremmel M., Roth N., Peiris H. V., Saintonge A., Volonteri M., Quinn T., Governato F., 2017, *MNRAS*, **465**, 547
- Pratt G. W., Arnaud M., Biviano A., Eckert D., Ettori S., Nagai D., Okabe N., Reiprich T. H., 2019, *Space Sci. Rev.*, **215**, 25
- Rafelski M., et al., 2015, *AJ*, **150**, 31
- Rasia E., et al., 2014, *ApJ*, **791**, 96
- Roediger E., et al., 2015, *ApJ*, **806**, 104
- Rubin K. H. R., Diamond-Stanic A. M., Coil A. L., Crighton N. H. M., Moustakas J., 2018, *ApJ*, **853**, 95
- Sanchez N. N., Werk J. K., Tremmel M., Pontzen A., Christensen C., Quinn T., Cruz A., 2018, arXiv e-prints,
- Sandage A., Binggeli B., Tammann G. A., 1985, *AJ*, **90**, 1759
- Shen S., Wadsley J., Stinson G., 2010, *MNRAS*, **407**, 1581
- Stinson G., Seth A., Katz N., Wadsley J., Governato F., Quinn T., 2006, *MNRAS*, **373**, 1074
- Stocke J. T., Keeney B. A., Danforth C. W., Shull J. M., Froning C. S., Green J. C., Penton S. V., Savage B. D., 2013, *ApJ*, **763**, 148
- Stocke J. T., Keeney B. A., Danforth C. W., Oppenheimer B. D., Pratt C. T., Berlind A. A., Impey C., Jannuzi B., 2019, *ApJS*, **240**, 15
- Tejos N., et al., 2016, *MNRAS*, **455**, 2662
- Tepper-García T., Richter P., Schaye J., Booth C. M., Dalla Vecchia C., Theuns T., 2012, *MNRAS*, **425**, 1640
- Tonnesen S., Bryan G. L., van Gorkom J. H., 2007, *ApJ*, **671**, 1434
- Toomre A., Toomre J., 1972, *ApJ*, **178**, 623
- Tremmel M., Governato F., Volonteri M., Quinn T. R., 2015, *MNRAS*, **451**, 1868
- Tremmel M., Karcher M., Governato F., Volonteri M., Quinn T. R., Pontzen A., Anderson L., Bellovary J., 2017, *MNRAS*, **470**, 1121
- Tremmel M., et al., 2019, *MNRAS*, **483**, 3336
- Tripp T. M., et al., 2011, *Science*, **334**, 952
- Tumlinson J., et al., 2011, *ApJ*, **733**, 111
- Tumlinson J., et al., 2013, *ApJ*, **777**, 59
- Tumlinson J., Peebles M. S., Werk J. K., 2017, *ARA&A*, **55**, 389
- Turk M. J., Smith B. D., Oishi J. S., Skory S., Skillman S. W., Abel T., Norman M. L., 2011, *ApJS*, **192**, 9
- Urban O., Werner N., Allen S. W., Simionescu A., Mantz A., 2017, *MNRAS*, **470**, 4583
- Vazza F., Eckert D., Simionescu A., Brüggén M., Ettori S., 2013, *MNRAS*, **429**, 799
- Wadsley J. W., Stadel J., Quinn T., 2004, *New Astron.*, **9**, 137
- Wadsley J. W., Veeravalli G., Couchman H. M. P., 2008, *MNRAS*, **387**, 427
- Wadsley J. W., Keller B. W., Quinn T. R., 2017, *MNRAS*, **471**, 2357
- Walker S., et al., 2019, *Space Sci. Rev.*, **215**, 7
- Wang Q. D., Walker S., 2014, *MNRAS*, **439**, 1796
- Wang Q. D., Owen F., Ledlow M., 2004, *ApJ*, **611**, 821
- Werk J. K., Prochaska J. X., Thom C., Tumlinson J., Tripp T. M., O'Meara J. M., Peebles M. S., 2013, *ApJS*, **204**, 17
- Werk J. K., et al., 2014, *ApJ*, **792**, 8
- Werner N., Urban O., Simionescu A., Allen S. W., 2013, *Nature*, **502**, 656
- White S. D. M., Rees M. J., 1978, *MNRAS*, **183**, 341
- Yoon J. H., Putman M. E., 2013, *ApJ*, **772**, L29
- Yoon J. H., Putman M. E., 2017, *The Astrophysical Journal*, **839**, 117
- Yoon J. H., Putman M. E., Thom C., Chen H.-W., Bryan G. L., 2012, *ApJ*, **754**, 84
- Zhuravleva I., Churazov E., Kravtsov A., Lau E. T., Nagai D., Sunyaev R., 2013, *MNRAS*, **428**, 3274
- Zinger E., Dekel A., Birnboim Y., Kravtsov A., Nagai D., 2016, *MNRAS*, **461**, 412
- Zinger E., Dekel A., Kravtsov A. V., Nagai D., 2018, *MNRAS*, **475**, 3654
- van de Voort F., Schaye J., Booth C. M., Dalla Vecchia C., 2011, *MNRAS*, **415**, 2782